Hindawi
International Journal of Antennas and Propagation
Volume 2022, Article ID 2923367, 12 pages
https://doi.org/10.1155/2022/2923367

Research Article

Analysis of Transmission Characteristics on an MSK-Based Rotating Magnet-Based Mechanical Antenna

Xie He, Qiang Zhou, and Jianya Zhang

The Sixty-Third Research Institute, National University of Defense Technology, Nanjing 210007, China

Correspondence should be addressed to Qiang Zhou; zhouqiang63@nudt.edu.cn

Received 6 June 2022; Revised 20 July 2022; Accepted 28 July 2022; Published 25 August 2022

Academic Editor: Shobhit K. Patel

A rotating magnet-based mechanical antenna (RMBMA) is a new promising paradigm which can significantly reduce both the size and the power consumption of the super-low frequency electromagnetic transmitter. To further reveal the effects of the rotational motion on transmission, this paper investigates the performance analysis of MSK (Minimum Shift Keying)-based RMBMA for the first time. Initially, based on the framework of MSK-based RMBMA, both the information loading of RMBMA and the control strategies of the motor are proposed, such that the impacts of the step response induced by the motor on the information loading are characterized. Then, the transmission capacity of the MSK-based RMBMA is derived in the closed form. The results indicate that increasing output torque or decreasing inertia load can enhance the transmission capacity. Finally, numerical simulations using a realistic system model demonstrate the validity of the proposed performance analysis. The simulation results show that when the inertia is less than 0.0128 kg•m^2 and the symbol rate is less than 4 bit/s, the bit error rate is less than 10%, thereby improving the transmission capacity. The proposed comprehensive design principles of RMBMA provide guidance for system design and practical implementation.

1. Introduction

Super-low frequency (SLF, 30–300 Hz) waves have the characteristics of long propagation distance and good seawater penetration, which have great potential for applications in the field of underwater communication [1–4]. However, the low-frequency electromagnetic transmitting antennas of existing technologies are all electrically small antennas (ESAs), which rely on the oscillating current in the conductor to excite electromagnetic waves. There is a Chu–Harrington limit [5–9], making its transmitting system to have features of bulky size, low radiation efficiency, high transmitting power, and energy consumption, which restricts the development of low-frequency electromagnetic communication in related fields.

To solve the above problems, the US Defense Advanced Research Projects Agency (DARPA) put forward the concept of the mechanical antenna (MA) in December 2016 and launched the AMEBA (a mechanically based antenna) project in August 2017 [10]. It is a new low-frequency electromagnetic transmitting technology that directly excites electromagnetic waves through the mechanical movement of special materials (such as electrets or permanent magnets) [11–14]. Benefiting from the mature application of rare Earth permanent magnet materials [15] and rotating drive technology [16] in various fields, the rotating magnet-based MA (RMBMA) attracts domestic and foreign attention. RMBMA can generate a static magnetic field directly without consuming energy, and there is no high-reactance problem and additional loss. Thus, RMBMA, connected with the motion excitation and control technology of low loss and low damping, can achieve low-frequency electromagnetic waves and information loading at the cost of little energy. It is expected to break through the Chu–Harrington limit of traditional low-frequency ESA [17].

The information loading of RMBMA is realized in the mechanical drive link which means the loaded information is transformed into the control signal of the drive motor. In recent years, the information loading method of RMBMA

has been studied. In [18], the modulation of magnetic field amplitude is introduced, which changes the magnetoresistance of the shielding mechanism near the permanent magnet. But the increase of shielding weakens the magnetic field intensity, which is not conducive to the improvement of transmission distance. In [19], the RMBMA technology scheme and information loading method for FSK (Frequency Shift Keying) and MSK (Minimum Shift Keying) are proposed. A prototype is developed to verify the feasibility of FSK modulation, but no quantitative analysis of the transmission performance is performed. In [20], a method based on continuous frequency FSK is introduced, which minimizes the additional torque for the motor to maintain the required bit rate, ensuring that the additional torque is limited to a finite concentration. The driving requirement is reduced, which contributes to the reduction of transmitter power consumption. In summary, the current research on the information loading method of RMBMA is mainly focused on the principle verification of the information modulation method. However, there are few investigations into rotating drives, control performance, and transmission characteristics.

Therefore, this paper aims to reveal the influence relationship between the steady-state and transient performance of the rotating servo system and the transmission characteristics of RMBMA. Based on [19], the MSK-based information loading and driving control strategy of RMBMA is introduced. The transmission characteristic analytical method is proposed, and the transceiver link simulation model is established.

2. System Model of RMBMA

RMBMA is a typical electromechanical coupled system, and according to the conversion relationship among electricity, mechanic, and magnetism energy, the system model of RMBMA is established, as shown in Figure 1. The spinning magnet acts as the load of the servo system, overcoming the frictional damping and moment of inertia and rotating with the permanent magnet synchronous motor (PMSM). The induced/radiated electromagnetic field can be equivalently generated by induction/radiation damping R_{rad}. A part of the mechanical energy is converted into radiated electromagnetic energy; hence, the mechanical motion equation of the spinning magnet can be expressed as

$$T_{em} = J_m \frac{d\Omega}{dt} + R_{\Omega 1}\Omega + R_{rad}\omega, \quad (1)$$

where T_{em} is electromagnetic torque, $R_{\Omega 1}$ is frictional damping, ω is the angular frequency; J_m, Ω, and N are the moment of inertia, rotational angular velocity, and pole pairs of the spinning magnet, respectively, and $N = \omega/\Omega$. As shown in Figure 2, the induced/radiated electromagnetic energy in the incident direction r is received by the magnetic antenna after superimposing the channel noise in the transmission channel. The magnetic antenna is equal to an induction coil hinging on a time-varying magnetic field whose output-induced voltage U [21] can be expressed as follows:

$$U = 2\pi N_0 S f B \cos\theta', \quad (2)$$

where N_0 and S are the numbers of turns and the cross-sectional area of the coil, respectively, f is the excitation electromagnetic wave frequency, B is the received magnetic field intensity, and θ' is the angle between the axis of the coil and the r direction ($\theta' = 0^\circ$ indicates that the coil axis is horizontal).

3. Information Loading and Control Strategy Using MSK

The rotational state of the spinning magnet cannot be changed abruptly due to the rotational inertia, and the modulated waveform is required to have constant amplitude and continuous phase to reduce distortion, so MSK is used as the information loading method of RMBMA. For an MSK signal, the k_{th} symbol can be expressed as [22]:

$$s_k(t) = A\cos\left(2\pi f_c t + \theta_k(t)\right) kT_{RB} < t \le (k+1)T_{RB}, \quad (3)$$

where A is the amplitude, f_c is the carrier frequency, $\theta_k(t)$ is the additional phase of the k_{th} symbol, $T_{RB} = 1/R_B$ is the symbol time, and R_B is the symbol rate.

The rotational speed n of the spinning magnet corresponds to the excitation electromagnetic wave frequency f, and the rotation angle Θ (rotor position P) corresponds to the phase θ of the excitation electromagnetic wave. Figure 3 gives the diagram of the rotating speed and rotor position control signals generated from the symbol. Here, $n/f = \Delta n/\Delta f = 60N$; P is equal to θ and always changes $\pm\pi/2$ within a symbol time T_{RB}, i.e., linearly increases $\pi/2$ when the symbol is 1 and linearly decreases $\pi/2$ when the symbol is 0.

As shown in Figure 4, the control loop of PMSM [23] corresponding to the MSK signal is introduced, which mainly consists of the automatic speed regulator (ASR) and the automatic current regulator (ACR). In the rotating speed control, the ASR obtains the given current of the current loop I_q^* based on the error between the given speed n^* and the calculated actual speed n. The ACR adjusts the output voltage of the power converter in real time to control the output torque of the motor based on the vector control strategy with zero direct shaft current [24] and finally achieves a fast and high-precision tracking response to the given speed. The rotor position control is realized by the magnetic coding current [25], and it changes the output voltage of the power converter in real time based on the estimated rotor position information and the input given signal according to the adaptive control strategy [26] so that the rotor tracks the input given signal. Thus, the information loading for MSK signals can be achieved by implementing real-time control for n and P.

4. Analysis of Transmission Characteristics

4.1. Effect of Spinning Magnet Parameters on Amplitude. The physical model of the spinning magnet is equated to a rotating magnetic dipole and can be regarded as two orthogonal vibrating magnetic dipoles with the same frequency in the same plane [27]. The time-varying

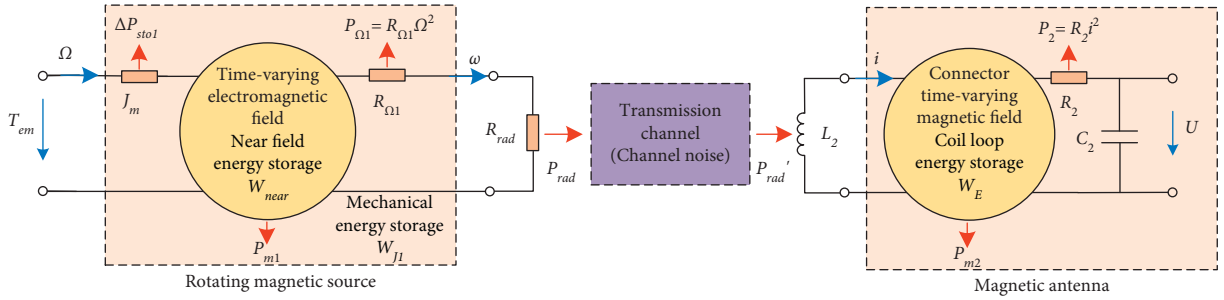

Figure 1: System model and energy conversion of RMBMA.

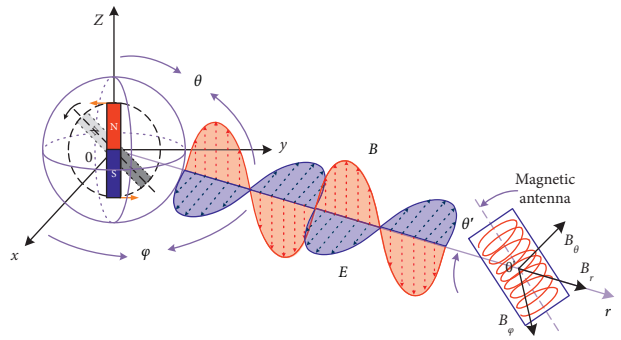

Figure 2: Diagram of the magnetic antenna receiving electromagnetic waves.

electromagnetic field component generated by a spinning magnet in a uniform lossy medium can be expressed as

$$\mathbf{B}_M = -\frac{\mu_0 m_0 \gamma^3}{4\pi} e^{-j\gamma r} \left\{ 2\left[j\left(\frac{1}{\gamma r}\right)^2 + \left(\frac{1}{\gamma r}\right)^3 \right] (\cos\theta + j \sin\theta \sin\varphi)\hat{r} - \left[\left(\frac{1}{\gamma r}\right) - j\left(\frac{1}{\gamma r}\right)^2 - \left(\frac{1}{\gamma r}\right)^3 \right] [(\sin\theta - j\cos\theta \sin\varphi)\hat{\theta} - j\cos\varphi\hat{\boldsymbol{\varphi}}] \right\}, \tag{4}$$

where μ_0 is the magnetic permeability, r is the propagation distance, $m_0 = VB_r/\mu_0$ is the magnetic moment of the magnet (V is the volume of the magnet, and B_r is the remanence), $\hat{r}$, $\hat{\theta}$, $\hat{\varphi}$ are the unit vectors in the direction of r, θ, and φ, *respectively*, $\gamma = \beta - j\alpha$ is the wave number of the lossy medium, and α and β are the attenuation and phase shift factors, respectively.

$$\alpha = \sqrt{\omega^2 \frac{\mu_0 \varepsilon}{2} \cdot \sqrt{1 + \left(\frac{\sigma}{\omega\varepsilon}\right)^2} - 1},$$
$$\beta = \sqrt{\frac{\omega^2 \mu_0 \varepsilon}{2} \cdot \sqrt{1 + \left(\frac{\sigma}{\omega\varepsilon}\right)^2} + 1}, \tag{5}$$

where ε and σ are the dielectric constant and conductivity, respectively. Assuming that the magnetic antenna is placed in the r direction and the angle θ' with the r direction is 0°, the magnetic field intensity of the hinge of the induction coil can be expressed as

$$\mathbf{B}_0 = \frac{\mu_0 m_0}{2\pi r^3} e^{-j\gamma r} \cdot [j(\gamma r) + 1] \cdot \hat{r}. \tag{6}$$

To simplify the analysis, assuming that the permanent magnet is a cylinder and the material is NdFeB ($\rho = 7800$ kg/m^3 is the density), its outer diameter and height are R and h, respectively, the rotational inertia $J_m = MR^2/2$, $M = \rho V$ is the mass of the magnet, and $V = \pi R^2 h$ is the volume of the magnet. When B_0 is constant, the aspect ratio $\lambda = h/R$ (the structure of the magnet) is changed by changing J_m when the receiving distance is certain. The rotational inertia $J_m = 0.0032$ kg·m^2 ($V = 500$ cm^3 and $\lambda = 2.4$) is taken as the ideal value [28, 29] in this paper.

4.2. Effect of Rotational Motion on Frequency. Due to the rotational inertia of both the spinning magnet and the rotor, abrupt speed variation is not allowed. As shown in

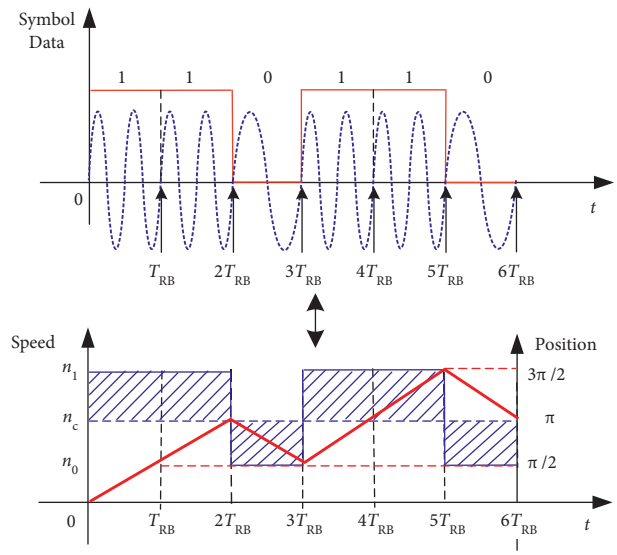

FIGURE 3: Rotating speed and rotor position control corresponding to the MSK signal.

Figure 5, the MSK modulation signal in turn appears as the speed step change. Therefore, the steady-state and dynamic performance of the servo system determines the transmission characteristics of RMBMA. Assuming $N = 1$, $n_c/f_c = \Delta n/\Delta f = 60$ and $\Omega = \omega = (\pi/30)n$, particularly, for MSK, $\Delta n = 15/T_{RB}$, $\Delta f = 1/(4T_{RB})$. It can be seen that the given speed increases suddenly from 60 $(f_0 - 1/(4T_{RB}))$ to 60 $(f_0 + 1/(4T_{RB}))$ at t_1, and it decreases suddenly from 60 $(f_0 + 1/(4T_{RB}))$ to 60 $(f_0 - 1/(4T_{RB}))$ at $t_1 + T_{\mathrm{RB}}$. The corresponding rotation angular velocity is $\Omega_1 \sim \Omega_2$ at $t_1 \sim t_1 + \Delta t_r$. For the drive characteristics of PMSM, T_{em} is constant [30], since $T_{em} \gg (R_\Omega + R_{rad})\Omega$, $d\Omega/dt$ is approximately a constant from equation (1). Hence, the transient process of the speed step change can be regarded as a linear variation, and the times reaching stable performance are Δt_r and Δt_f, respectively (ignoring the oscillation process).

Neglect the higher-order oscillation process, the angular velocity whose step-change response is approximated as a linear rise and decay process in Figure 5 can be expressed as

$$\Omega = \begin{cases} \dfrac{\pi}{T_{RB}\Delta t_r} t + \Omega_c - \dfrac{\pi}{2T_{RB}} - \dfrac{\pi t_1}{T_{RB}\Delta t_r} t_1 \sim t_1 + \Delta t_r, \Omega_c + \dfrac{\pi}{2T_{RB}} t_1 + \Delta t_r \sim t_1 + T_{RB}, \\ -\dfrac{\pi}{T_{RB}\Delta t_f} t + \Omega_c + \dfrac{\pi}{2T_{RB}} + \dfrac{\pi(t_1 + T_{RB})}{T_{RB}\Delta t_f} t_1 + T_{RB} \sim t_1 + T_{RB} + \Delta t_f, \\ \Omega_c - \dfrac{\pi}{2T_{RB}} t_1 + T_{RB} + \Delta t_f \sim t_1 + 2T_{RB}. \end{cases} \tag{7}$$

Since $n/f = \Delta n/\Delta f = 60$, frequency has the same variation as angular velocity. Then, neglecting the effects of $R_{\Omega 1}$ and R_{rad} in (1), for the rise and decay processes in Figure 5, we have

$$\begin{cases} J_m \displaystyle\int_{\Omega_1}^{\Omega_2} \mathrm{d}\Omega \approx \int_{t_1}^{t_1 + \Delta t_r} T_{em} \mathrm{d}t \Rightarrow \frac{2\Delta\Omega f}{\Delta t_r} = \frac{4\pi\Delta f}{\Delta t_r} = \frac{\pi R_B}{\Delta t_r} \approx \frac{T_{em}}{J_m} \text{ speed increasing}, \\ J_m \displaystyle\int_{\Omega_2}^{\Omega_1} \mathrm{d}\Omega \approx \int_{t_1 + T_{\mathrm{RB}}}^{t_1 + T_{\mathrm{RB}} + \Delta t_f} T_{em}' \mathrm{d}t \Rightarrow -\frac{2\Delta\Omega f}{\Delta t_f} = -\frac{4\pi\Delta f}{\Delta t_f} = -\frac{\pi R_B}{\Delta t_f} \approx -\frac{T_{em}'}{J_m} \text{ speed decreasing}. \end{cases} \tag{8}$$

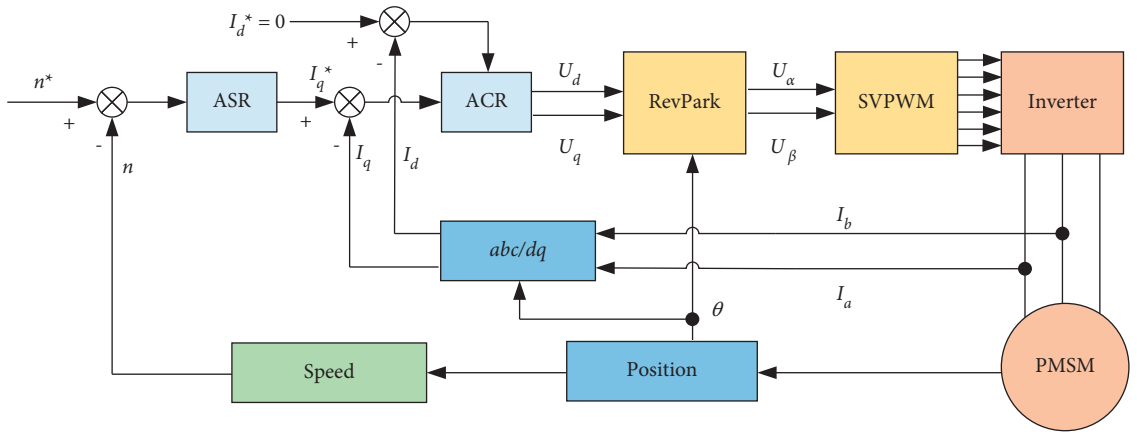

Figure 4: Control loop of the PMSM corresponding to the MSK signal.

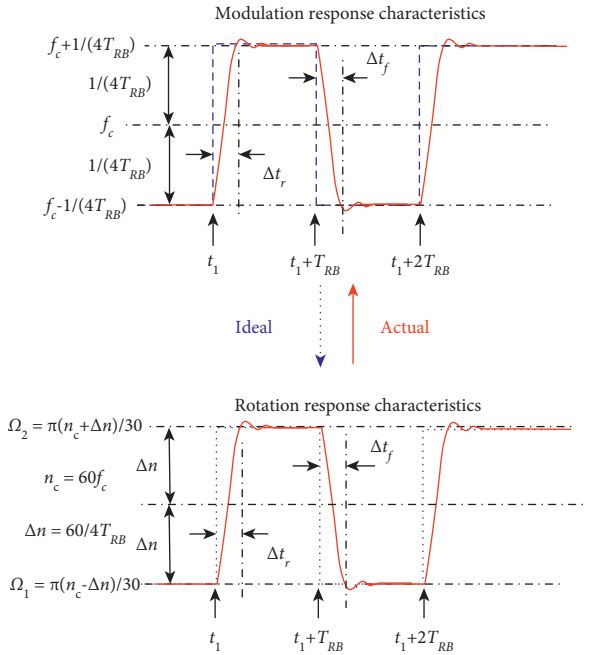

Figure 5: Speed step response of RMBMA.

where $\Delta\Omega=(\pi/30)\bullet\Delta n$, T'_{em} is the braking torque.$T'_{em}=0$ indicates that PMSM drives without a brake control mode, and $\Delta t_f \gg \Delta t_r$. To reduce the drive loss and avoid an excessive difference between Δt_f and Δt_r, the feedback braking control strategy [31] is adopted. The rotor mechanical energy is converted into electrical energy and fed back to the DC bus through boosting, which can make T_{em} and T'_{em} approximately equal while recovering the braking energy.

4.3. Effect of Rotational Motion on Phase. The amount of change in the additional phase is equal to the actual rotational angular velocity of the spinning magnet minus the integral amount of the unmodulated rotational angular velocity. For the step response process shown in Figure 5, supposing the initial phase at t_1 is 0, $\theta_k(t)$, then the additional phase difference $\Delta\theta_k(t)$ can be expressed as

$$\theta_k(t) = \begin{cases} \dfrac{\pi\Delta t_r}{2T_{RB}} t_1 \sim t_1 + \Delta t_r, \\ \dfrac{\pi}{2T_{RB}}(t-t_1)t_1 + \Delta t_r \sim t_1 + T_{RB}, \\ \dfrac{\pi}{2} t_1 + T_{RB} \sim t_1 + T_{RB} + \Delta t_f, \\ \pi + \dfrac{\pi\Delta t_f}{2T_{RB}} - \dfrac{\pi}{2T_{RB}}(t-t_1)t_1 + T_{RB} + \Delta t_f \sim t_1 + 2T_{RB}, \end{cases} \tag{9}$$

$$\Delta\theta_k(t) = \begin{cases} \dfrac{\pi(\Delta t_r + t_1 - t)}{2T_{RB}} t_1 \sim t_1 + \Delta t_r, \\ 0\, t_1 + \Delta t_r \sim t_1 + T_{RB}, \\ \dfrac{\pi(t - t_1 - T_{RB})}{2T_{RB}} t_1 + T_{RB} \sim t_1 + T_{RB} + \Delta t_f, \\ \dfrac{\pi\Delta t_f}{2T_{RB}} t_1 + T_{RB} + \Delta t_f \sim t_1 + 2T_{RB}. \end{cases} \tag{10}$$

It can be seen that the amount of change of $\theta_k(t)$ at the rise and decay process is 0 from (9), which means $\theta_k(t)$ behaves as a period of Δt_r or Δt_f time delay at the rise and decay process, and the change of phase within a T_{RB} is no longer $\pm\pi/2$. As shown in Figure 6, if $\Delta t_r \neq \Delta t_f$, the phase error increases continuously with the accumulation of time, and if the control strategy is adopted, i.e., $\Delta t_r = \Delta t_f$, the phase error generated in the previous rise/decay process will be compensated in the next rise/decay process, and there is no longer a cumulative error.

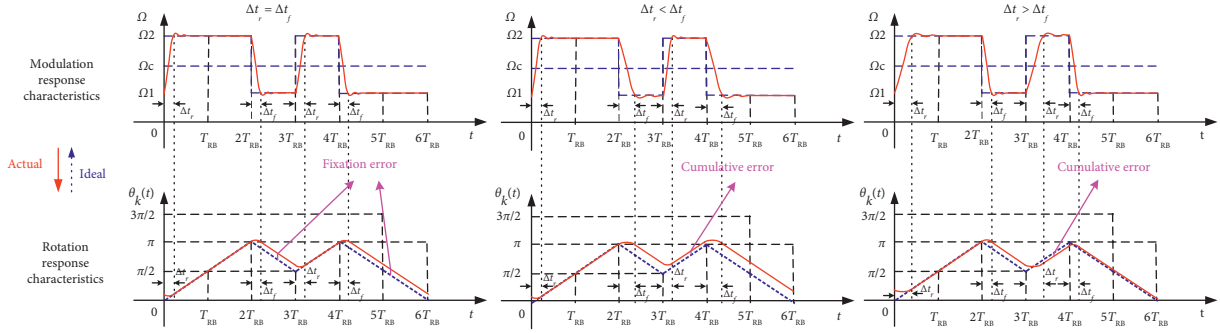

Figure 6: Phase change of RMBMA.

4.4. Effect of Rotational Motion on Transmission Performance. For MSK signals with bandwidth $B_w = 1/T_{RB}$, assuming $\Delta t = \Delta t_r = \Delta t_f$, the transmission performance is analyzed in terms of transmission capacity ($B_W R_B$), which can be expressed according to (7) as

$$B_w R_B = R_B^2 \approx K_{SNR} \cdot \left(\frac{T_{em}}{J_m}\right). \tag{11}$$

With

$$K_{SNR} = \left(\frac{1}{\pi}\right)\left(\frac{\Delta t}{T_{RB}}\right). \tag{12}$$

K_{SNR} is inversely correlated with SNR, which reflects signal distortion of about $\Delta t/T_{RB}$. The signal distortion is generated by the frequency step response and phase fixation error introduced by rotational motion, and the smaller Δt or K_{SNR} is, the higher the SNR value is. When K_{SNR} is small, the signal distortion is mainly outside the band, which has a little effect on the in-band signal and is not easy to occur symbol error; when $K_{SNR} > 1/\pi$, the phase error generated in the previous rise/decay process cannot be compensated in the next rise/decay process, and the phase accumulation error occurs, which affects the in-band signal and is bound to occur bit error; when K_{SNR} is small and remains unchanged, the transmission capacity of RMBMA ($B_w R_B$) is proportional to T_{em}/J_m, that is, the transmission capacity can be improved by increasing the output torque or decreasing the inertia.

5. Simulation Validation

5.1. Transmitter and Transceiver Link Modelling Based on MSK. The transmission characteristics of RMBMA are determined by two aspects: the output field intensity and the rotating servo performance of the rotating permanent magnet. Corresponding to the signal amplitude of receiving distance, and the transient response process of frequency and phase, respectively. For channel noises are white Gaussian noises, the transmitter and receiver link modes are established as shown in Figure 7.

The transmitter link model offers five modules: MSK signal generation, magnetic field distribution model [27], structural design and stress field analytical model [28], electromagnetic field analytical model of PMSM [32], and servo control model. According to the correspondence shown in Figure 3, the MSK signal generation module converts the input symbol data into the given speed. As required for receiving distance and field intensity, the magnetic moment m_0 is calculated by the magnetic field distribution model, then the spinning magnet structure and size are determined by the structural design and stress field analytical model, and the rotational inertia of the spinning magnet is obtained. With the PMSM parameters, the PMSM electromagnetic field analytical model calculates its output electromagnetic torque T_{em}. The servo control model adjusts the actual speed with reference to the given speed. Finally, the simulation waveform $B(t)$ of RMBMA output magnetic field strength is obtained by the magnetic field intensity simulation of the spinning magnet.

The receiver link converts the electromagnetic wave $B(t)$ output from the transmitting link into the induced voltage $U(t)$ of the induction coil after superimposing a certain amount of noise power on it. From (2), $U(t)$ is proportional to $f(t)$, so no coherent demodulation of $B'(t)$ can be achieved by extracting the envelope of $U(t)$. The received chip data are obtained after envelope detection, shaping filtering, and normalization, and finally, the bit error rate (BER) is analyzed.

5.2. Simulation Results. MATLAB is used for the simulation of the proposed structure. The PMSM parameters are cited from [28] with the rated speed at 60,000 rpm, $T_{\text{em}} = 0.8$ N•m. Based on the above transmitter and transceiver link model, MSK modulation is adopted, and the transmission characteristics of RMBMA are simulated and analyzed by adjusting the rotational servo control parameters and the rotational inertia J_m of the spinning magnet. Taking $f_c = 300$ Hz, $\Delta f = 1$ Hz, $R_B = 4$ bit/s, and $J_m = 0.0032$ kg•m^2, a feedback braking control strategy is used, and its effect is adjusted by ACR. The speed step response of the spinning magnet corresponding to different feedback braking effects is shown in Figure 8. The fall time ($\Delta t_{f1} = 45.70$ ms) for speed from 18060 rpm to 17940 rpm is much larger than the rise time ($\Delta t_{r1} = 9.72$ ms) for speed from 17940 rpm to 18060 rpm when the feedback braking effect is poor, and Δt_{r2} and Δt_{f2} are equal to 9.72 ms when the feedback braking control effect is good.

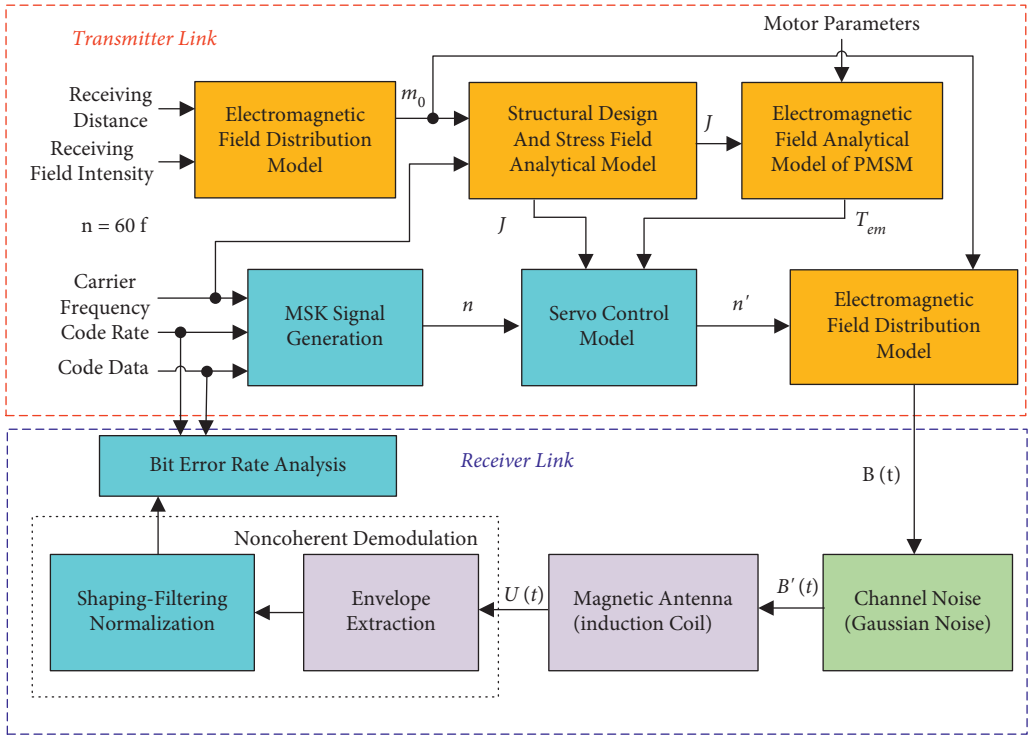

Figure 7: Transmitter and receiver link model of RMBMA.

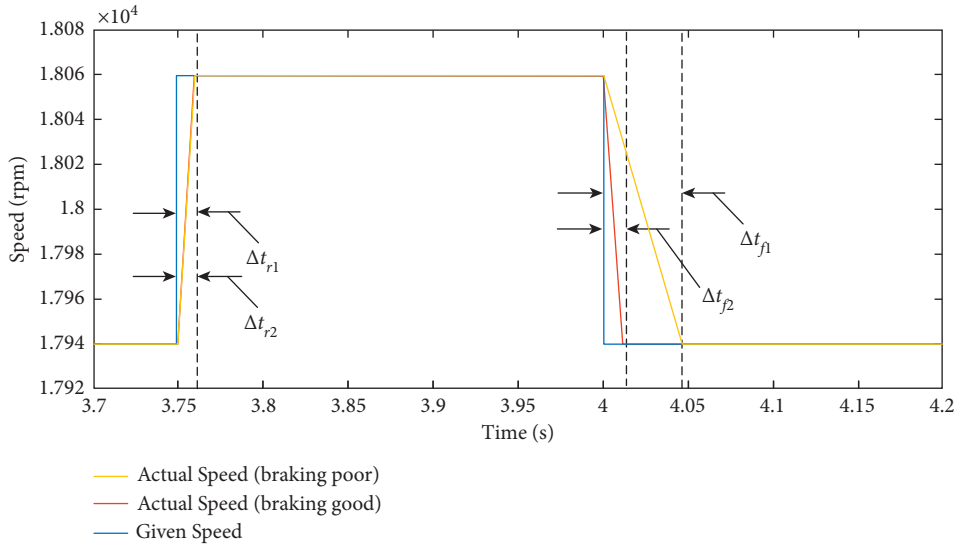

Figure 8: Speed step response diagram of RMBMA.

Removing the speed rise time of the PMSM, the phase change is observed in a steady state. The simulated comparison of the phase and spectrum change corresponding to different feedback braking effects is shown in Figure 9. From Figure 9(a), it can be seen that when the feedback braking effect is poor ($\Delta t_r < \Delta t_f$), the cumulative error of the phase keeps increasing with time. When the feedback braking control effect is good ($\Delta t_r = \Delta t_f$), the phase error is only shown as a fixation error in the decay process, and there is no more cumulative error. From Figure 9(b), From Figure 9(b), it can be seen that whether Δtr and Δtf are equal has little effect on the in-band signal spectrum. But harmonic components is appeared in $f_c \pm k\Delta f$ (k is odd and $k>1$) when $\Delta t_r < \Delta t_f$ (green), causing out-band distortion.

When the magnetic moment is constant, changing the rotational inertia J_m affects the structure of the magnet.

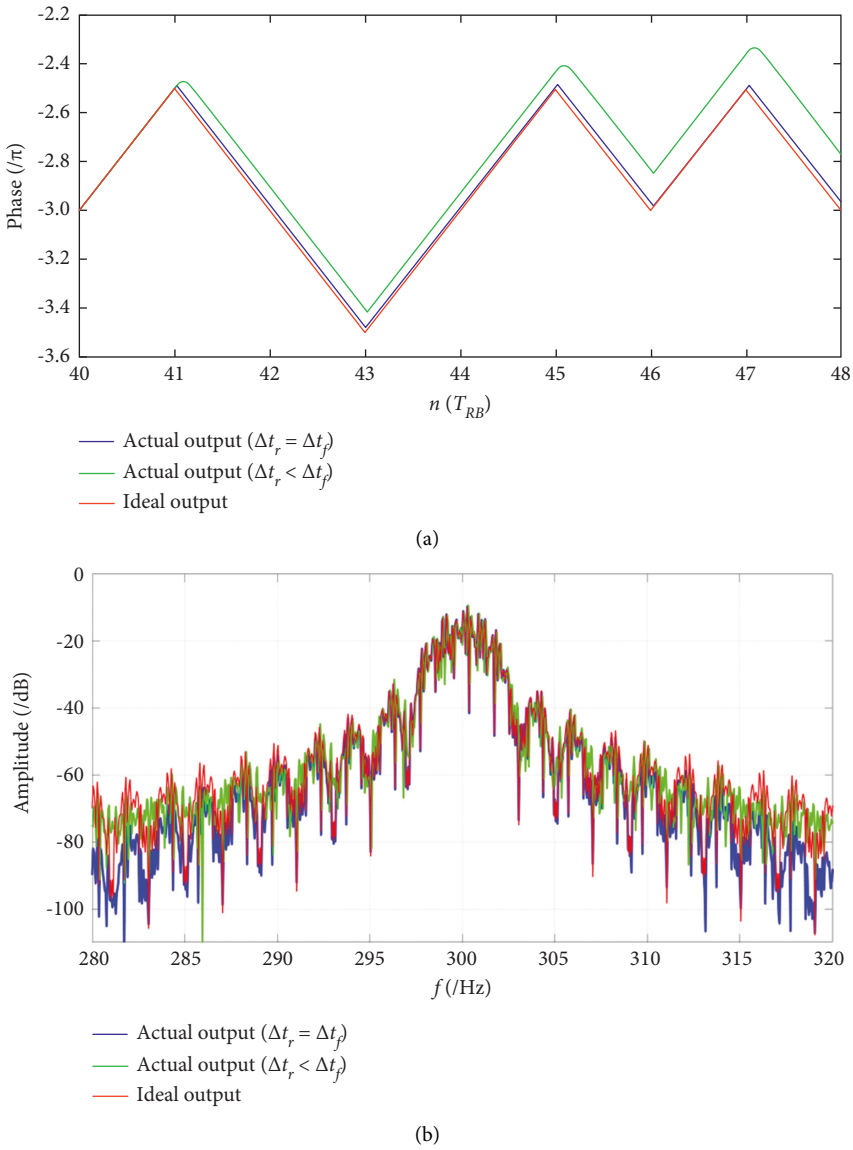

Figure 9: Simulation results of the phase and spectrum affected by different feedback braking effects (a) phase; (b) output signal spectrum.

Taking $f_c = 300$ Hz, $\Delta f = 1$ Hz, and $R_B = 4$ bit/s, the feedback braking control strategy is adopted and keeps a good braking effect so that $\Delta t_r \approx \Delta t_f$. The simulation results of the phase and spectrum with different inertias are shown in Figure 10. It can be seen that when J_m is small, Δt_r and Δt_f are much smaller than T_{RB}, the fixation error of phase is small, and there is no accumulated error, which has a little effect on the in-band signal spectrum and mainly introduces out-band distortion; when J_m is large, the error of phase increases with Δt_r and Δt_f getting increased, and the introduced distortion increases accordingly. Especially when Δt_r and Δt_f are nearing or over T_{RB}, the error of phase is no longer the previous fixed value, and the accumulated error is generated instead. The in-band distortion is introduced, and the error bit is generated. The same as that revealed by (11) and (12), the transmission capacity of RMBMA is inversely proportional to J_m.

For $\Delta f = 1/(4T_{RB})$ and $T_{RB} = 1/R_B$, changing the symbol rate R_B affects Δf. Taking $f_c = 300$ Hz and $J_m = 0.0032$ kg•m^2, the feedback braking control strategy is adopted and keeps a good braking effect so that $\Delta t_r \approx \Delta t_f$. The simulation results of the phase and spectrum for $R_B = 2$ bit/s($\Delta f = 0.5$ Hz), $R_B = 4$ bit/s($\Delta f = 1$ Hz), and $R_B = 8$ bit/s($\Delta f = 2$ Hz) are shown in Figures 11 and 12. It can be seen that as R_B*increases,* Δt_r and Δt_f increase, leading to an increase in the fixed error of the phase. When R_B is small, the increase in the fixation error of the phase has a little effect on the in-band signal spectrum; when R_B increases, T_{RB} decreases, and the decrease of the out-band signal power increases as R_B. Especially when Δt_r and Δt_f are nearing or over T_{RB}, the fixation error of the phase has an effect on the in-band signal spectrum, and the error bit is generated, which is the same as that revealed by equation (12).

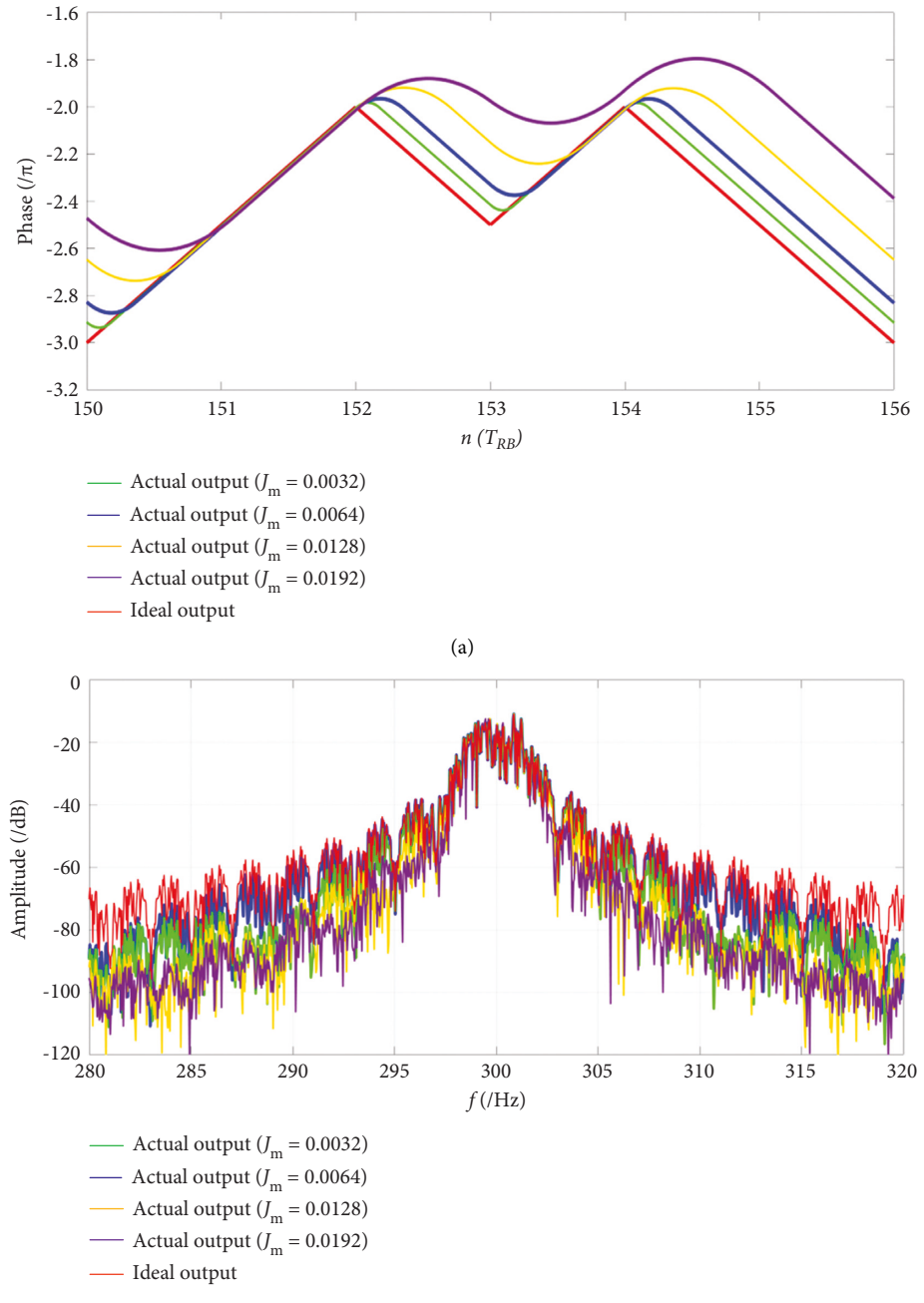

Figure 10: Simulation results of the phase and spectrum affected by different inertias (a) phase; (b) output signal spectrum.

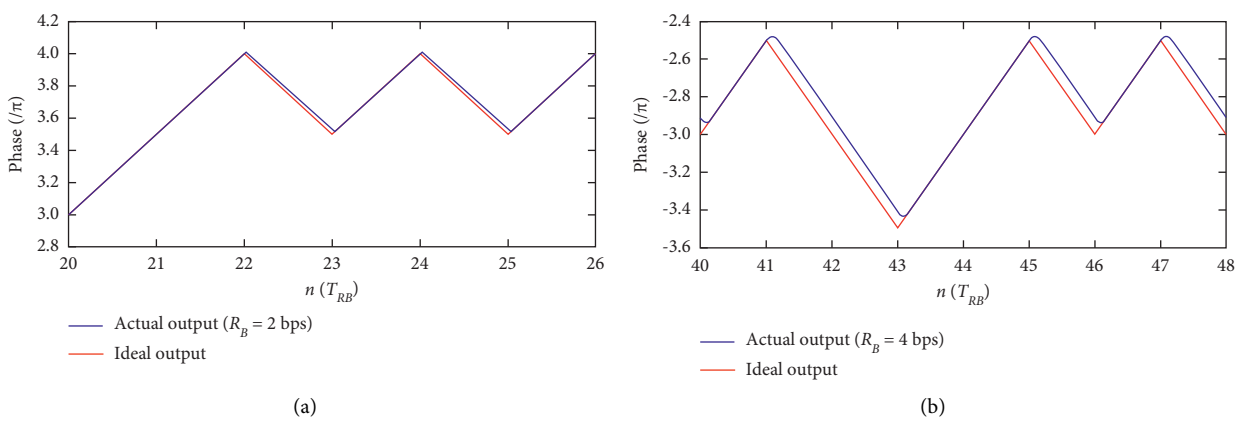

Figure 11: Continued.

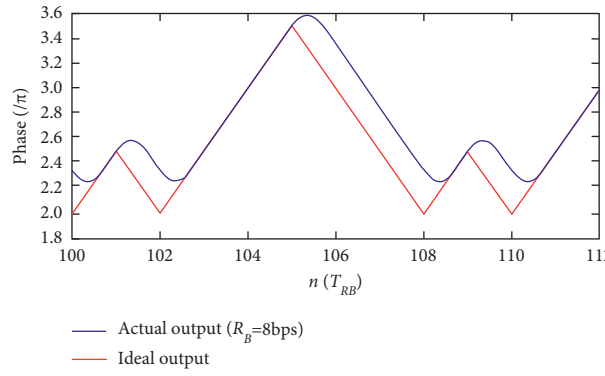

(c)

FIGURE 11: Simulation results of the phase and spectrum affected by different symbol rates (a) $R_B = 2$ bit/s ($\Delta(f) = 0.5$ Hz); (b) RB = 4 bit/s ($\Delta(f) = 1$ Hz); (c) RB = 8 bit/s ($\Delta(f) = 2$ Hz).

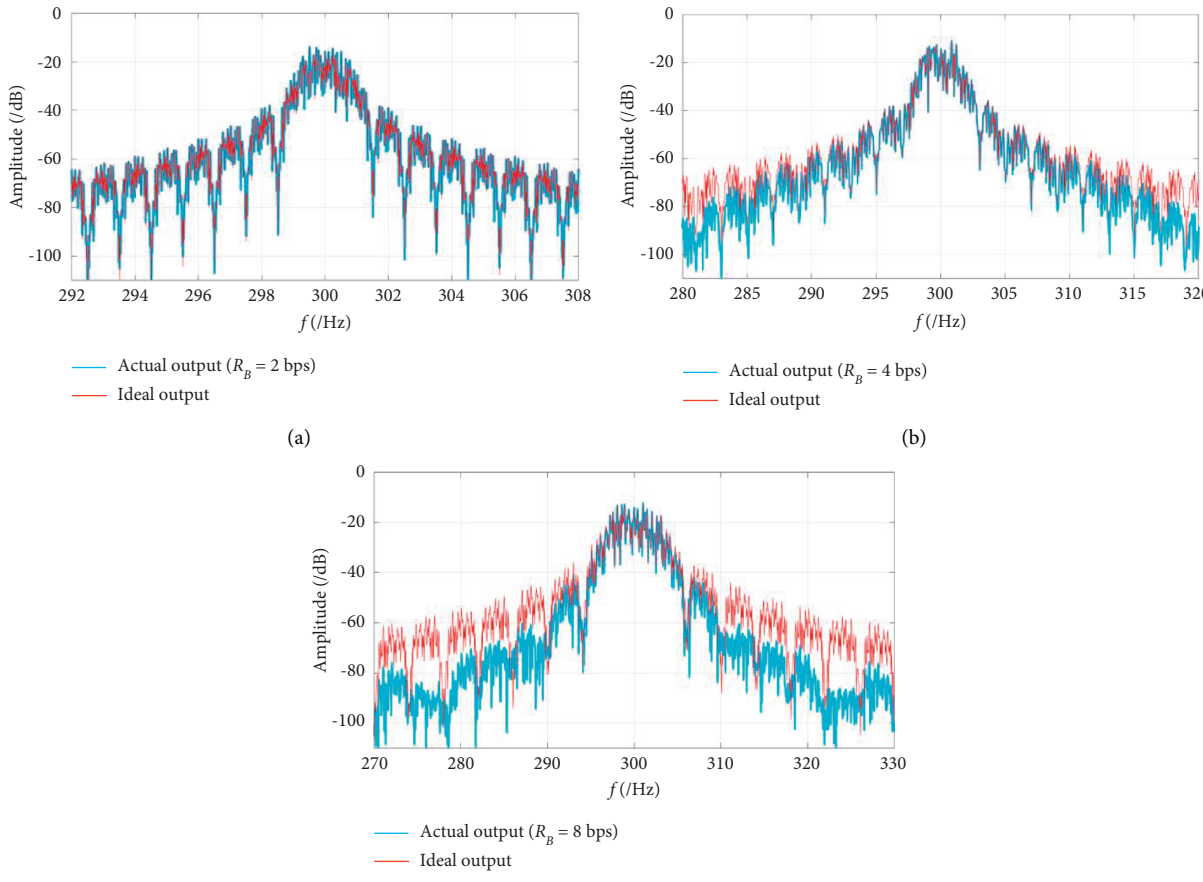

(c)

FIGURE 12: Simulation results of the phase and spectrum affected by different symbol rates (a) $R_B = 2$ bit/s ($\Delta(f) = 0.5$ Hz); (b) RB = 4 bit/s ($\Delta(f) = 1$ Hz); (c) RB = 8 bit/s ($\Delta(f) = 2$ Hz).

According to the transmitter and transceiver link mode introduced in Figure 7, the BER is analyzed with different symbol rates and inertias. Having $f_c = 300$ Hz, the simulation results of the BER with no coherent demodulation are shown in Figure 13. In the light of Figure 13(a), $R_B = 4$ bit/s ($\Delta f = 1$ Hz), when $J_m \geq 0.0128\,\text{kg}\cdot\text{m}^2$, and Δt_r and Δt_f are nearing or over T_{RB}. When the symbol data change, the bit error easily appears, of which the BER is greater than 10^{-1}. Moreover, Δt_r and Δt_f decrease with the decrease of J_m, resulting in the decline of the BER for MSK signals. From

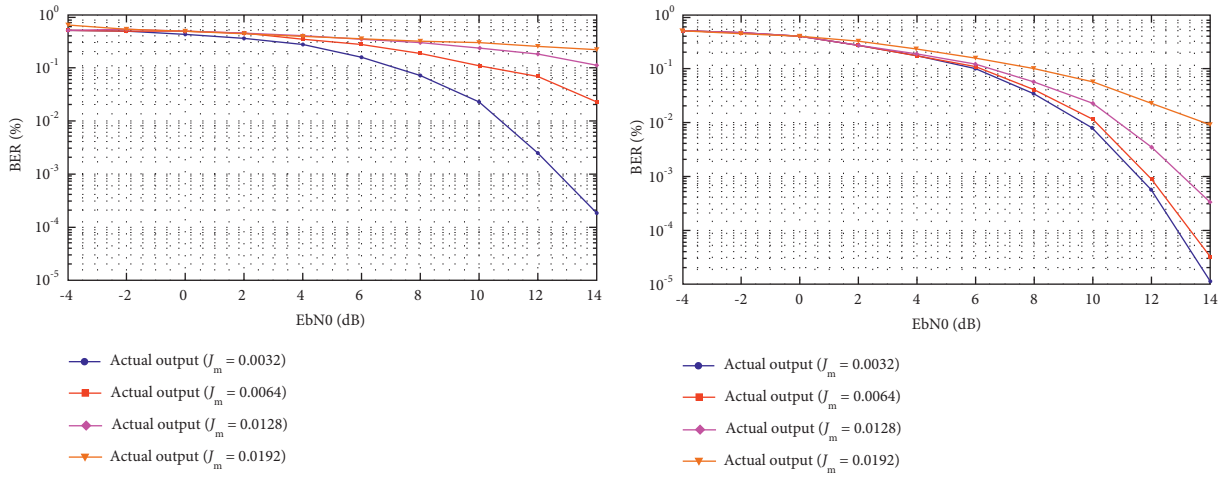

FIGURE 13: Simulation results of the bit error rate with noncoherent demodulation (a) $R_B = 2$ bit/s ($\Delta(f) = 0.5$ Hz); (b) RB = 4 bit/s (Δ(f) = 1 Hz).

Figure 13(b), when J_m is larger, the BER reduces with the decrease of R_B.

6. Conclusions

In this paper, the information loading and driving control strategy for MSK modulation-based RMBMA is introduced, and the transient response analytical method of transmission characteristics is proposed. The transmission capacity of RMBMA is proportional to T_{em}/J_m for MSK signals. The greater the output torque and the less the inertia load are, the higher the permitted transmission capacity is for a certain SNR. The transmission characteristics of RMBMA with MSK modulation are simulated and analyzed. The frequency step change fits the speed step change of the spinning magnet. However, there is a transient transition time of the speed step change, corresponding to the stable time of the frequency step change and the phase error, due to the spinning magnet inertia. It has a direct influence on signal quality and receiving BER. In practical applications, transmission performance can be enhanced by designing PMSM with big enough torque. To reduce harmonic distortion, a suitable control strategy should be adopted to ensure the rise/decay process times Δt_r and Δt_f of the step change are equal and much smaller than T_{RB}. In order to reduce the BER and improve the transmission capacity, the symbol rate should be less than 4 bit/s, and the inertia should be less than 0.0128 kg•m^2.

Data Availability

The data used to support the findings of this study are included within the article.

Conflicts of Interest

The authors declare that they have no conflicts of interest.

Acknowledgments

This work was supported in part by the National Natural Science Foundation of China (Project 61971431) and the Scientific Research Plan Important Supporting Project of National University of Defense Technology (ZK 17-02-02).

References

[1] N. Barani and K. Sarabandi, "Mechanical antennas: emerging solution for very-low frequency (VLF) communication," in *Proceedings of the 2018 IEEE International Symposium on Antennas and Propagation*, pp. 95-96, Boston, MA, USA, January 2018.

[2] J. A. Bickford, A. E. Duwel, M. S. Weinberg, R. S. McNabb, D. K. Freeman, and P. A. Ward, "Performance of electrically small conventional and mechanical antennas," *IEEE Transactions on Antennas and Propagation*, vol. 67, no. 4, pp. 2209–2223, April 2019.

[3] T. K. Nguyen, S. K. Patel, S. Lavadiya, and C. Danh Bui, *Design and Fabrication of Multiband Reconfigurable Copper and Liquid Multiple Complementary Split-Ring Resonator Based Patch Antenna*, , pp. 1–24, WAVES IN RANDOM AND COMPLEX MEDIA, 2022.

[4] S. P. Lavadiya, S. K. Patel, and R. Maria, "High gain and frequency reconfigurable copper and liquid metamaterial tooth based microstrip patch antenna," *AEU-International Journal of Electronics and Communications*, vol. 137, Article ID 153799, 2021.

[5] L. J. Chu, "Physical limitations of omni-directional antennas," *Journal of Applied Physics*, vol. 19, no. 12, pp. 1163–1175, 1948.

[6] R. F. Harrington, "Effect of antenna size on gain, bandwidth, and efficiency," *Journal of Research of the National Bureau of Standards, Section D: Radio Propagation*, vol. 64, p. 1, 1960.

[7] J. S. McLean, "A re-examination of the fundamental limits on the radiation Q of electrically small antennas," *IEEE Transactions on Antennas and Propagation*, vol. 44, no. 5, p. 672, 1996.

[8] K. Vasu Babu, S. Das, G. N. J. Sree, S. K. Patel, M. Pardha Saradhi, and M. Tagore, "Design and development of

miniaturized MIMO antenna using parasitic elements and Machine learning (ML) technique for lower sub 6 GHz 5G applications," *AEU-International Journal of Electronics and Communications*, vol. 153, Article ID 154281, 2022.

[9] K. V. Babu, S. Das, G. N. J. Sree, B. T. P. Madhav, S. K. K. Patel, and J. Parmar, "Design and optimization of micro-sized wideband fractal MIMO antenna based on characteristic analysis of graphene for terahertz applications," *Optical and Quantum Electronics*, vol. 54, no. 5, p. 281, 2022.

[10] S. Gong, Yu Liu, and Yi Liu, "A Rotating-magnet based mechanical antenna (RMBMA) for ELF-ULF wireless communication," *Progress in Electromagnetics Research M*, vol. 72, pp. 125–133, 2018.

[11] Q. Zhou, F. Q. Yao, W. Shi et al., "Research on mechanism and key technology of mechanical antenna for a low-frequency transmission," *Sci Sin Tech*, vol. 50, no. 1, pp. 69–84, 2020.

[12] O. C. Fawole and M. Tabib-Azar, "Electromechanically-modulated permanent magnet antennas of wireless communication," in *Proceedings of the 2017 IEEE Sensors*, pp. 1–3, Glasgow, UK, December 2017.

[13] Y. Cui, M. Wu, Z. Y. Li et al., "A miniaturized mechanical antenna based on FEP/THV unipolar electrets for extremely low frequency transmission," *Microsystems & Nanoengineering*, vol. 8, no. 1, p. 58, 2022.

[14] Y. Niu and H. Ren, "Transceiving signals by mechanical resonance: a miniaturized standalone low frequency (lf) magnetoelectric mechanical antenna pair with integrated DC magnetic bias," *IEEE Sensors Journal*, vol. 22, no. 14, pp. 14008–14017, 2022.

[15] Y. Luo, "Development of NdFeB magnet industry in new century," *Journal of Iron and Steel Research, International*, vol. 13, pp. 1–11, 2006.

[16] J. F. Gieras, "High speed machines," in *Advancements in Electric Machines. Power Systems*Springer, Dordrecht, 2008.

[17] M. N. S. Prasad, Y. K. Huang, and E. Wang, "Going beyond Chu Harrington limit: ULF radiation with a spinning magnet array," in *Proceedings of the 32nd General Assembly and Scientific Symposium of the International Union of Radio Science*, Montreal, QC, Canada, November 2017.

[18] N. D. Strachen, J. H. Booske, and N. Behdad, "Mechanical super-low frequency (SLF) transmitter using electrically-modulated reluctance," in *Proceedings of the 2018 IEEE International Symposium on Antennas and Propagation & USNC/URSI National Radio Science Meeting*, pp. 67-68, Boston, MA, USA, January 2018.

[19] Q. Zhou, W. Shi, and B. Liu, "Research and practice of the mechanical antennas based on rotating permanent magnet (in Chinese)," *Journal of National University of Defense Technology*, vol. 42, no. 3, pp. 128–136, 2020.

[20] J. S. Glickstein, J. Liang, S. Choi, A. Madanayake, and S. Mandal, "Power-efficient ELF wireless communications using electro-mechanical transmitters," *IEEE Access*, vol. 8, pp. 2455–2471, 2020.

[21] X. Wang, W. Zhang, X. Zhou, Z. Cao, and X. Quan, "Research on permanent magnet-type super-low-frequency mechanical antenna communication," *International Journal of Antennas and Propagation*, vol. 2021, Article ID 5524732, 16 pages, 2021.

[22] J. G. Proakis, *Digital Communication*, McGraw-Hill Book Co, New york, 2021.

[23] J. F. Pan, Y. Zou, G. Cao, N. C. Cheung, and B. Zhang, "High-precision dual-loop position control of an asymmetric bilateral linear hybrid switched reluctance motor," *IEEE Transactions on Magnetics*, vol. 51, no. 11, pp. 1–5, 2015.

[24] K. Hruska and P. Dvorak, *Optimization of a PMSM Design for Control with Zero Direct axis Current Component*, in *Proceedings of the 2016 ELEKTRO*, pp. 162–167, Strbske Pleso, Slovakia, July 2016.

[25] B.-J. Kang and C.-M. Liaw, "A robust hysteresis current-controlled PWM inverter for linear PMSM driven magnetic suspended positioning system," *IEEE Transactions on Industrial Electronics*, vol. 48, no. 5, pp. 956–967, Oct. 2001.

[26] C. C. Chan, F. Xue, J. Wu, and W. C. Lo, "Sliding-mode controlled induction motor drive using gain-adaptive phase-locked loop speed control IECON'99," in *Proceedings of the Conference Proceedings. 25th Annual Conference of the IEEE Industrial Electronics Society (Cat. No.99CH37029)*, vol. 2, pp. 608–613, San Jose, CA, USA, August 1999.

[27] W. Shi, Q. Zhou, and B. Liu, "Performance analysis of spinning magnet as mechanical antenna (in Chinese)," *Acta Physica Sinica*, vol. 68, no. 18, pp. 308–318, 2019.

[28] H. Zheng, X. Li, Z. Hao, Q. Zhou, and W. Long, "Design of a high-speed permanent magnet motor with a spinning magnet source for mechanical antenna," in *Proceedings of the IEEE 9th International Power Electronics and Motion Control Conference (IPEMC2020-ECCE Asia)*, pp. 154–159, March 2020.

[29] W. Shi, Q. Zhou, and B. Liu, "The Performance Analysis of a Spinning Magnet as a Mechanical Antenna," in *Proceedings of the 2019 Photonics & Electromagnetics Research Symposium - Fall (PIERS - Fall)*, pp. 1265–1269, Xiamen, China, March 2019.

[30] J. Kim, I. Jeong, K. Lee, and K. Nam, "Fluctuating current control method for a PMSM along constant torque contours," *IEEE Transactions on Power Electronics*, vol. 29, no. 11, pp. 6064–6073, 2014.

[31] B. W. Harini, A. Subiantoro, and F. Yusivar, "Study of speed sensorless permanent magnet synchronous motor (PMSM) control problem due to braking during steady state condition," in *Proceedings of the 2017 15th International Conference on Quality in Research (QiR): International Symposium on Electrical and Computer Engineering*, pp. 184–189, Nusa Dua, Bali, Indonesia, December 2017.

[32] Z. Kolondzowski, *Thermal and Mechanical Analyses of High-Speed Permanent-Magnet Electrical Machines*, tkk dissertations, Finland, 2010.